Materials Advances

PAPER

View Article Online
View Journal | View Issue

Check for updates

Cite this: *Mater. Adv.*, 2026, 7, 495

Selective cellular uptake and cytotoxicity effects of fluorescent carbon dots: a comparative study in cancer and normal cells

Ankesh Kumar,[a] Raghu Solanki,[a] Geethu Prakash,[a] Abdulkhalik Mansuri,[a] Ashutosh Kumar,[b] Dhiraj Bhatia*[a] and Pankaj Yadav*[c]

Cancer remains one of the most critical global health challenges. Early detection is crucial for effective treatment and improved patient survival. However, conventional diagnostic tools often struggle to identify cancer in its early stages due to limitations such as low sensitivity, high costs, and a reliance on tumor size. Additionally, commercial dyes used for imaging face challenges like poor water solubility, toxicity, instability, and high cost, making them expensive and imprecise in targeting early-stage tumors. In recent years, carbon dots (CDs) have emerged as promising fluorescent imaging probes thanks to their nanoscale size, adjustable surface properties, strong fluorescence, and excellent biocompatibility, which make them suitable for various biological applications, including bioimaging, drug delivery, and tissue engineering. In this study, green, fluorescent carbon dots (GCDs) were synthesized using citric acid and ascorbic acid as carbon sources through a reflux method at 130 °C for 12 hours. The prepared GCDs were characterized using dynamic light scattering (DLS), atomic force microscopy (AFM), high-resolution transmission electron microscopy (HR-TEM), UV-vis spectroscopy, fluorescence spectrophotometry, X-ray photoelectron spectroscopy (XPS), and Fourier-transform infrared (FTIR) analysis, including an assessment of their stability. We evaluated cellular uptake and cytotoxicity in both cancer and normal cell lines, finding that the resulting GCDs exhibited nanoscale size, strong photostability, and low toxicity. Importantly, we analysed the optical properties and stability of the GCDs and compared cellular uptake with fluorescein isothiocyanate (FITC), as well as the fluorescence intensity of both GCDs and FITC in normal and cancer cells. The GCDs were more significantly internalised by cancer cells (MDA-MB-231 breast cancer cells and HeLa cervical cancer cells) compared to normal cells (RPE1 retinal pigment epithelial cells, HEK293T human embryonic kidney cells, and NIH-3T3 mouse embryo cells). Additionally, we explored the potential of GCDs in zebrafish models. This selective uptake led to increased accumulation. In conclusion, our findings highlight the cost-effective and eco-friendly development of GCDs, which show promising potential for cancer bioimaging and theranostic applications.

Received 20th July 2025,
Accepted 27th October 2025

DOI: 10.1039/d5ma00781j

rsc.li/materials-advances

1. Introduction

Cancer ranks as the second leading cause of death worldwide. Early detection of the disease significantly enhances treatment success, increases survival rates, reduces complications, and lowers healthcare costs.[1] In 2022, almost 20 million people were diagnosed with cancer, leading to about 9.7 million deaths.[2,3] One in five will develop cancer, with one in nine men and one in twelve women expected to die from it in their lifetime. Among men, the most prevalent types of cancer include lung, prostate, colorectal, stomach, and liver cancer, whereas breast, colorectal, lung, cervical, and thyroid cancers are the most common for women.[4]

Chemotherapy, radiotherapy and immunotherapy are the common cancer treatments and have higher success rate when the disease is detected early.[1] Early identification leads to improved survival rates, reduced morbidity, and lower treatment costs. For early cancer detection, various dyes are available for cancer detection,[5] including fluorescein sodium,[6] methyl blue,[7] and indocyanine green (ICG).[8] However, these dyes come with their own set of limitations, such as low fluorescence, poor water

---

[a] *Department of Biological Sciences and Engineering, Indian Institute of Technology Gandhinagar, Palaj, Gujarat, 382355, India. E-mail: dhiraj.bhatia@iitgn.ac.in*
[b] *Biological and Life Sciences, School of Arts & Sciences, Ahmedabad University, Central Campus, Navrangpura, Ahmedabad, Gujarat, 380009, India*
[c] *Department of Biotechnology, School of Energy Technology, Pandit Deendayal Energy University, pdpu road, Raisan, Gandhinagar, Gujarat, 382421, India. E-mail: Pankaj.Y@spt.pdpu.ac.in*

solubility, cytotoxicity, instability, complicated synthesis processes, and high costs.[9] In addition, antibody-based fluorophores are used for early cancer detection. One notable example is the anti-CEA antibody,[10] which effectively stains gastric and colorectal tissues by targeting the carcinoembryonic antigen[11] (CEA) present in cancer cells. Another example is the NIR fluorescence dye (BM-105), which helps to localise tumours, offering essential guidance during surgical procedures. PSMA-targeted probes[12] represent an important category, specifically designed to target prostate cancer by binding to the prostate-specific membrane antigen (PSMA) found on cancer cells. These probes are valuable for both imaging and radiopharmaceutical therapy. However, antibody-based fluorophores do face challenges, including immunogenicity, delays in antigen identification, photobleaching, and high costs.[13–15] Enzyme receptor-based fluorophores also show promise for cancer detection. For instance, MMP-activatable[12] probes are used for breast cancer and are activated by matrix metalloproteinases (MMPs) that cleave peptide linkers, leading to a loss of FRET and subsequent fluorescence activation. Similarly, cathepsin-activatable probes[16] target cathepsin D, which cleaves a peptide substrate to release the BODIPY fluorophore, enabling pH-insensitive detection in lysosomes and phagosomes. Despite their potential, enzyme-based fluorophores also have limitations such as structural instability, complex synthesis, high cost and limited tissue penetration.[17]

Early detection of cancer can significantly reduce the death rate. However, this poses difficulties since the tumour needs to reach a detectable size. At present, cancer detection methods primarily rely on imaging techniques such as computed tomography (CT),[18] X-ray,[19] magnetic resonance imaging (MRI),[20] and ultrasound,[21] which encounter challenges including high radiation exposure, low signal-to-noise ratios, and high costs. Therefore, there is a pressing need for the development of more effective and novel approaches for the early detection of cancer.[22] Fluorescent nanoparticles offer a more effective means of selectively targeting cancerous cells. The advancement of novel nanoparticle-based fluorophores should have characteristics such as high photostability, biocompatibility, easy synthesis, and excellent fluorescence to differentiate between cancerous and normal cells.[23]

In recent years, fluorescent nanoparticles have gained significant attention due to their unique properties.[24] Among them, carbon dots (CDs) stand out due to their excellent optical characteristics, such as biocompatibility, excellent photostability, strong fluorescence, easy synthesis, and cost-effectiveness.[25–27] CDs are emerging nanoparticles with a size range of 2–10 nm and a quasi-spherical shape and morphology. Their remarkable fluorescence was first reported during the purification of single-walled carbon nanotubes in 2004, which sparked interest in their use for bioimaging applications. Several studies have reported the development of modified CDs capable of distinguishing between normal and cancer cells. A key factor influencing the higher uptake of CDs in cancer cells is the tumor microenvironment, characterized by leaky blood vessels and poor lymphatic drainage.[28] This facilitates higher accumulation of core–shell CDs in tumour tissues *via* a passive targeting mechanism, which is less effective in healthy tissues. Additionally, the negatively charged membranes of cancer cells, attributed to the excessive presence of phosphatidylserine, can enhance interactions with CDs designed with zwitterionic or pH-responsive surfaces.[29] These surface modifications may shift to positive charge in the acidic environment of tumors, resulting in greater cellular uptake. Moreover, cancer cells often overexpress specific transporters, such as LAT1 (L-type amino acid transporter 1),[30] allowing for the active internalization of CDs that are functionalized with amino acid mimics, a feature that normal cells do not possess. The metabolic profile of cancer cells, including elevated levels of glutathione (GSH), further enhances the fluorescence signal of CDs/Fe^{3+} complexes, facilitating more effective tumor imaging. In contrast, normal cells with lower GSH levels exhibit weaker fluorescence. Furthermore, the rapid proliferation rate of cancer cells leads to increased endocytic activity, significantly boosting CD internalization. For example, GCD nanocrystals exhibit four times higher fluorescence intensity in HeLa cancer cells compared to normal cells.[31] GCDs can be internalized by cells through various endocytic pathways: micropinocytosis, clathrin-mediated endocytosis, and caveolae-mediated endocytosis.[32]

In this study, we synthesised green, fluorescent carbon dots (GCDs) using citric acid and ascorbic acid as carbon sources *via* a reflux method. The synthesised GCDs were characterised using dynamic light scattering (DLS), atomic force microscopy (AFM), transmission electron microscopy (TEM), UV-vis spectroscopy, fluorescence spectrophotometry, Fourier transform infrared (FTIR) spectroscopy, and X-ray photoelectron spectroscopy (XPS). Cellular uptake studies and cell viability studies were conducted in both cancer and normal cell lines. Furthermore, the cellular uptake of GCDs and FITC in normal cells and cancer cells was compared and the fluorescence potential of GCDs in zebrafish was investigated. Our findings reveal that the GCDs exhibited significantly higher internalisation in cancer cells compared to normal cells. These results highlight the promising potential of GCDs for applications in bioimaging, drug delivery, cancer therapy and other biomedical fields.

2. Materials and methods

2.1. Materials

L-Ascorbic acid (99.5%) was sourced from Loba Chemicals. Citric acid anhydrous (extra pure) was purchased from SRL Chemicals. Ethanol (greater than 99.9%) and silicon oil were obtained from X-Chemicals, with the latter supplied by Changshu Hongsheng Fine Chemicals Co., Ltd. A 0.22-micrometre filter, along with a 3.5 kDa snakeskin membrane, was provided by Thermo Fisher. Milli-Q water was acquired from Merck Millipore. Cell culture dishes and dimethyl sulfoxide (DMSO) were obtained from HiMedia. Dulbecco's Modified Eagle Medium (DMEM), 0.25% trypsin-EDTA, and fetal bovine serum (FBS) were acquired from Gibco. Additional reagents included 4′,6-diamidino-2-phenylindole (DAPI) from Roche, Mowiol, MTT salt, 0.1% Triton X-100, 4% paraformaldehyde, and

Phalloidin A647 from Sigma Aldrich, Fluoresin (FITC), and E3 media. All reagents used were of analytical grade and required no further purification.

2.2. Synthesis of carbon dots (GCDs)

To synthesize GCDs, 1 g of ascorbic acid and citric acid were dissolved in a mixture containing twice the volume of distilled water and an equal volume of ethanol. The resulting solution was heated at 130 °C for 12 hours. After the reaction, the mixture was allowed to cool overnight. The resulting solution was collected in a 50 mL falcon tube and the pH was adjusted to 7 using 10 M NaOH. The mixture was then centrifuged at 10 000 rpm for 10 minutes at room temperature. The supernatant containing the GCDs was dialyzed against deionized water using a 3.5 kDa molecular weight cutoff dialysis membrane. Finally, the fluorescent GCDs were obtained by lyophilizing the dialyzed solution and collected into a 50 mL falcon tube.

2.3. Characterisation of the GCDs

The optical properties of the GCDs, including UV-vis absorbance and fluorescence emission, were measured using a Spectrocord-210 Plus (Analytokjena, Germany) and an FP-8300 Jasco spectrophotometer (Jasco, Japan), respectively. For UV-vis and fluorescence analysis, 200 μL of a 1 mg mL^{-1} GCD stock solution was diluted in 1 mL of Milli-Q water. After preparing the solution, 1 mL of the diluted sample was transferred into a quartz cuvette for analysis. The obtained data were plotted and analysed using Origin software.

For chemical structural analysis, the GCDs were lyophilised at pH 7 to obtain a dry powder. FTIR spectra were recorded in the range of 400 cm^{-1} to 4000 cm^{-1} using a PerkinElmer Spectrum Two spectrometer equipped with an ATR mode.

The elemental composition of the surface and the quantification of the GCDs were conducted using X-ray photoelectron spectroscopy (Thermo Scientific model K-Alpha). For the elemental composition analysis, 10 μL of a 1 mg mL^{-1} GCD stock solution was placed on a glass cover slip and allowed to dry overnight. The sample was then analysed, and the resulting data were plotted using Origin software.

Dynamic light scattering (DLS) was used for the solution-based size and charge characterisation of the GCQDs with a Malvern Analytical Zetasizer Nano ZS instrument. The data were then plotted using a Gaussian fit in OriginPro software.

The morphological characterisation was carried out using AFM and TEM. The samples were first dispersed at a concentration of 1 mg ml^{-1} in Milli-Q water and then 20 μL of this dispersion was further diluted in 1 mL of Milli-Q water. A 5 to 7 μL aliquot of the diluted sample was drop-cast onto the fresh mica sheet. The samples were dried in a vacuum desiccator. Imaging was carried out using a BIO-AFM (Bruker's Nanowizard Sense plus Bio-AFM) in tapping mode under ambient conditions. For the imaging process, a sharp silicon cantilever ScanAsyst-Air from Bruker was employed.

The samples were first dispersed at a concentration of 1 mg ml^{-1} in Milli-Q water and then 20 μL of this dispersion was further diluted in 1 mL of Milli-Q water. Then, 3 to 7 μL of the diluted sample was drop-cast onto a copper grid. The samples were dried in a vacuum desiccator. The TEM analysis was performed, and the data were analysed using ImageJ software, and the data were plotted using Origin software.

2.4. Cell culture

MDA-MB-231 (breast cancer cells), HeLa (cervical cancer cells), Rpe1 (retinal pigment epithelial cells), HEK293T (human embryonic kidney cells), and NIT3T3 (mouse NIH/Swiss embryo cells) were maintained in DMEM supplemented with 10% FBS and 1% penicillin–streptomycin, HEPES, sodium bicarbonate, and sodium pyruvate. The cells were kept at a temperature of 37 °C with 5% CO_2 in a humidified incubator.

2.5. Cellular uptake assay

RPE1 and MDA-MB231 cells were seeded on 10 mm coverslips placed in 4-well plates at a density of 3×10^5 cells per coverslip in DMEM supplemented with 10% FBS, 1× antibiotic mix (Penstrep), HEPES, sodium bicarbonate, and sodium pyruvate. The cells were grown for 24 hours at 37 °C in a 5% CO_2 atmosphere. The cells were treated with GCDs at concentrations of 0, 50, 100, and 200 μg mL^{-1} for 15 minutes. Post-treatment, the cells were fixed with 4% paraformaldehyde for 15 minutes at 37 °C, followed by three times with 1× PBS. The fixed cells were permeabilized using 0.1% Triton-X100 and stained with 0.1% phalloidin to visualize the actin filaments. After three additional washes with 1× PBS, the cells were mounted on slides with Mowiol containing DAPI for nuclei staining. Confocal imaging of the fixed cells was conducted using a Leica TCS SP8 confocal laser scanning microscope (CLSM, Leica Microsystem, Germany) with a 63× oil immersion objective. Image analysis was performed using Fiji (ImageJ).

2.6. *In vitro* cytotoxicity assessment of GCDs using the MTT assay

To evaluate the cytotoxic effects of the GCDs, approximately 1×10^4 RPE1 (retinal pigment epithelial) and MDA-MB-231 cells were seeded in a 96-well plate in 100 μl of complete growth media DMEM. The cells were incubated for 24 hours at 37 °C in a 5% CO_2 atmosphere to allow attachment. The following day, the cells were washed with PBS and treated with different concentrations of GCDs (10, 20, 30, 40, 50, 60, 70, 80, 90 and 100 μg mL^{-1}) for 24 hours. After treatment, the medium was removed, and 100 μl MTT reagent (5 mg mL^{-1}) was added and the cells were incubated for 3 to 4 hours. MTT solution was aspirated and 100 μL of DMSO was added to each well to dissolve the purple formazan crystals. Absorbance was measured at 565 nm using a Byonoy's Absorbance 96 microplate reader. All experiments were performed in triplicate and untreated cells were counted as the control to calculate the percentage of cell viability for each well. The untreated GCDs served as the control to determine the % cell viability of each well. The cell viability percentage was calculated using the following formula:

$$\text{Cell viability (\%)} = (\text{absorbance of the sample/absorbance of the control}) \times 100.$$

2.7. *In vivo* uptake study

In vivo uptake assays were conducted following the guidelines provided by the Organization for Economic Cooperation and Development (OECD). At 72 hours post-fertilisation (hpf), dead larvae were removed, and the remaining larvae were placed in 4-well plates (Corning, NY, USA), with 5 larvae in each well. The larvae were treated with green, fluorescent carbon at concentrations of 50, 100, and 200 μg mL^{-1} and incubated for 4 hours. One well was designated as a control, containing no GCDs. After treatment, the medium was replaced with fresh E3 media, and the larvae were washed to remove any excess GCDs. They were then fixed using a fixative solution (4% paraformaldehyde, PFA) for 2 minutes. Following fixation, the larvae were mounted with Mowiol mounting solution and allowed to dry before undergoing confocal imaging analysis. Ethical guidelines: the work was undertaken following the Guidelines of the Committee for the purpose of control and supervision of experiments on animals (CPCSEA), for experimentation on fishes in 2021. As per these regulations, the study is exempt from ethical and biosafety committee clearance.

2.8. Statistical analysis

Statistical evaluation was conducted utilising GraphPad Prism software (version 8.0.2). All data are presented as means ± standard deviation (SD) or means ± standard error derived from two independent experiments. *p*-Values were determined through one-way ANOVA and two-tailed unpaired Student's *t*-tests, with a confidence interval of 95%.

3. Results and discussion

3.1. Synthesis of GCDs

Citric acid and ascorbic acid were dissolved in a water–ethanol mixture (2 : 1 ratio) and subjected to reflux heating at 130 °C for 12 hours. After the reaction mixture cooled to room temperature, the pH was adjusted to 7 using 10 M NaOH. The solution was then centrifuged to remove any insoluble residues, and the supernatant was collected. This was followed by dialysis to remove small molecular impurities. Finally, the purified solution was lyophilized to obtain a dry carbon dot powder for further characterization and cell culture studies as illustrated in Fig. 1.

3.2. Characterisation of GCDs

3.2.1. UV spectroscopy and fluorescence spectroscopy. The optical properties of the synthesised GCDs were investigated using a UV-vis spectrophotometer and fluorescence spectroscopy. The UV-vis spectra exhibited a distinct absorption peak at 266 nm, which corresponds to the carbonic core centre. This band is attributed to the n–π^* transition of the C$\equiv$O bond, as shown in Fig. 2(a). The photoluminescence spectra revealed a maximum emission at 544 nm when excited at 450 nm, confirming the green fluorescence of the GCDs as shown in Fig. 2(b).

To further confirm their fluorescence properties, the GCDs were exposed to UV light. While no fluorescence was visible under daylight, the GCDs exhibited green fluorescence under UV illumination, resulting from electronic transitions within the carbon dots, as shown in Fig. 2(c).

3.2.2. Dynamic light scattering (DLS). Furthermore, DLS analysis revealed the hydrodynamic size distribution of the GCDs, with a dominant peak at ~3.9 nm indicating the average particle size, as shown in Fig. 2(d).

The surface charge of the GCDs was analysed by measuring the zeta potential using DLS at various pH levels: 2.74, 3.59, 7.0, and 10.3. The results indicated that when the pH increased, the zeta potential of the GCDs decreased, which reflects a reduction in surface charge. This trend suggests that at higher pH levels, the surface functional groups on the GCDs become less protonated. As a result, the surface exhibits either a lower positive

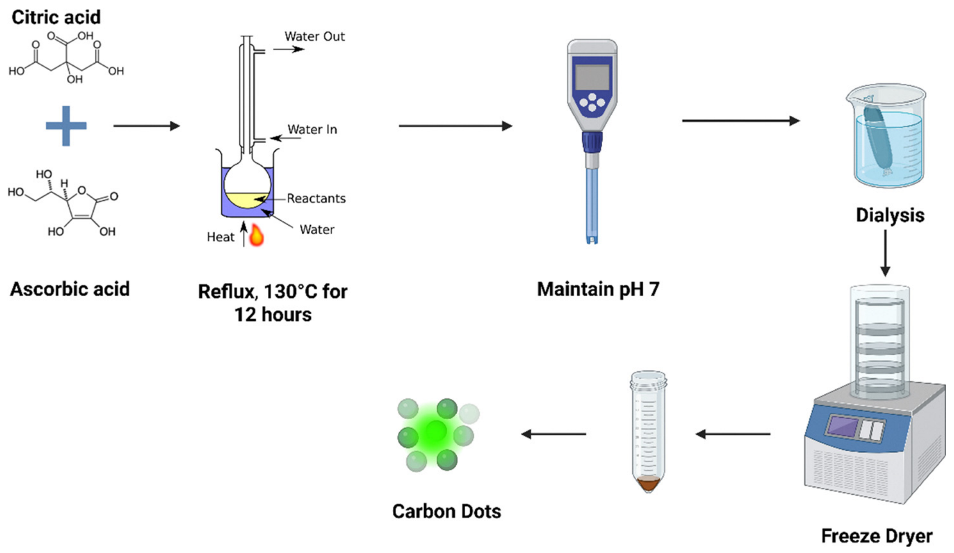

Fig. 1 Schematic representation of the synthesis of fluorescent GCDs.

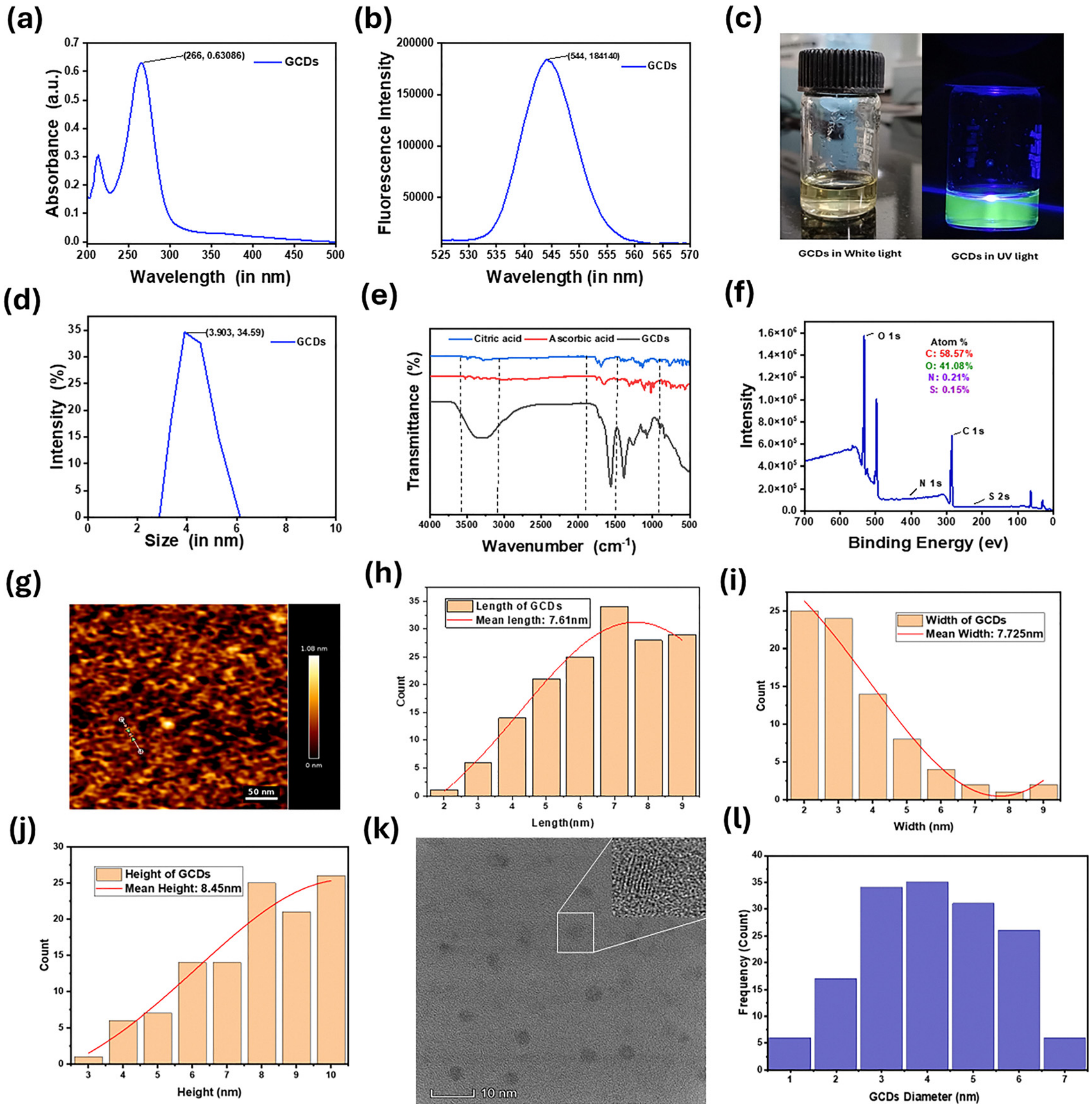

Fig. 2 Characterization of the GCDs: (a) UV-vis spectra and (b) fluorescence spectra of the GCDs. (c) The fluorescence of the GCDs is shown under room light (on the right) and UV light (on the left). (d) DLS and zeta potential analysis, where the *x*-axis represents size and the *y*-axis represents intensity. The FTIR spectrum and XPS spectrum are displayed as follows: (e) FTIR spectra, with the *x*-axis representing wavenumber and the *y*-axis representing transmittance (%). (f) XPS spectra, where the *x*-axis represents binding energy and the *y*-axis represents intensity. (g) AFM images and the distribution of GCDs (h)–(j), with a scale bar of 50 nm. The figures (h)–(j) show the count on the *y*-axis and length, height, and width on the *x*-axis. (k) High-resolution TEM images of GCDs, and (l) images representing the diameter of the GCDs.

Table 1 The zeta potential of the GCDs at different pH values

pH	2.74	3.59	7	10.3
Zeta potential (mV)	8.94 (+ve)	4.69 (+ve)	2.87 (+ve)	22.7 (−ve)

charge or an increased negative charge, depending on the specific ionizable groups present, as shown in Table 1.

3.2.3. FTIR and XPS. FTIR analysis was performed to determine the surface functionality of the citric acid, ascorbic acid and GCDs. FTIR spectra of the citric acid, ascorbic acid and GCDs displayed several characteristic absorption bands that indicate the presence of various functional groups. A peak around 2929 cm^{-1} corresponds to the O–H stretching vibration of carboxylic acids. The peak at 1564 cm^{-1} is attributed to C═C stretching in the aromatic rings and possibly N–H bending, suggesting the presence of aromatic and amine groups. Additionally, peaks at 1385 cm^{-1} and 1079 cm^{-1} corresponded to C–O stretching vibrations from alkoxy and phenol or acyl groups, respectively. The presence of alkenes and aromatic structures is further confirmed by bending vibrations at 911 cm^{-1} and 839 cm^{-1}, corresponding to alkene sp^2 C–H and aromatic sp^2 C–H bending. These features indicate that the GCDs contain carboxylic, aromatic, phenolic, alkene, and possibly amine functionalities, typical of functionalized carbon-based nanomaterials, as shown in Fig. 2(e).

The XPS spectra show that the prepared GCDs are overwhelmingly composed of carbon and oxygen (C: 58.57% and

O: 41.08%), with only trace nitrogen (N: 0.21%) and sulphur (S: 0.15.%). The spectrum displays a strong C 1s peak (typical ∼285 eV) and an even stronger O 1s signal (typical ∼530–533 eV), while small N 1s and S features confirm only minor heteroatom incorporation. This composition and the prominent oxygen signal indicate that the GCDs surfaces are rich in oxygen-containing groups (carboxyl, hydroxyl, carbonyl/epoxy-like functionalities), which explains their likely good aqueous dispersibility, hydrophilicity and ease of further chemical functionalization. The XPS spectra support that these GCDs are surface-oxidised, stable, and chemically accessible, as shown in Fig. 2(f).

3.2.4. AFM and TEM. AFM images, Fig. 2(g)–(j), showed the surface morphology and distribution of the GCDs. These images revealed that the GCDs are uniformly dispersed particles that exhibit a nearly spherical shape and smooth surface features. The mean size length, height, and width of the GCDs were 7.61, 8.45 and 7.72 nm, respectively, confirming that the size is >10 nm and the particles are spherical.

The high-resolution transmission electron microscopy (HRTEM) analysis indicates that the synthesised GCDs are uniformly dispersed, spherical, and free from aggregation, demonstrating good monodispersion and a scale bar of 10 nm. Fig. 2(k) includes an inset image that reveals distinct lattice fringes with an interplanar spacing of approximately 0.26 nm. The particle size distribution histogram shown in Fig. 2(l) indicates that the diameters of the GCDs range between 1 and 7 nm, with the majority clustered around 3–4 nm. These findings confirm that the GCDs are nanosized. Overall, the HRTEM results suggest that the prepared GCDs possess a well-defined core and size distribution.

3.2.5. Quantum yield and lifetime decay. The quantum yield (Φ) of the GCDs was calculated using rhodamine B as a reference. In a previous research article, the quantum yield for GCDs was found to be 3.3%. And the fluorescence lifetime of the GCDs was estimated in previous research work.[32] The lifetime decay of the GCQDs was calculated to be 30 ns; this short lifetime is due to the radiative recombination mechanism of luminescence.[32]

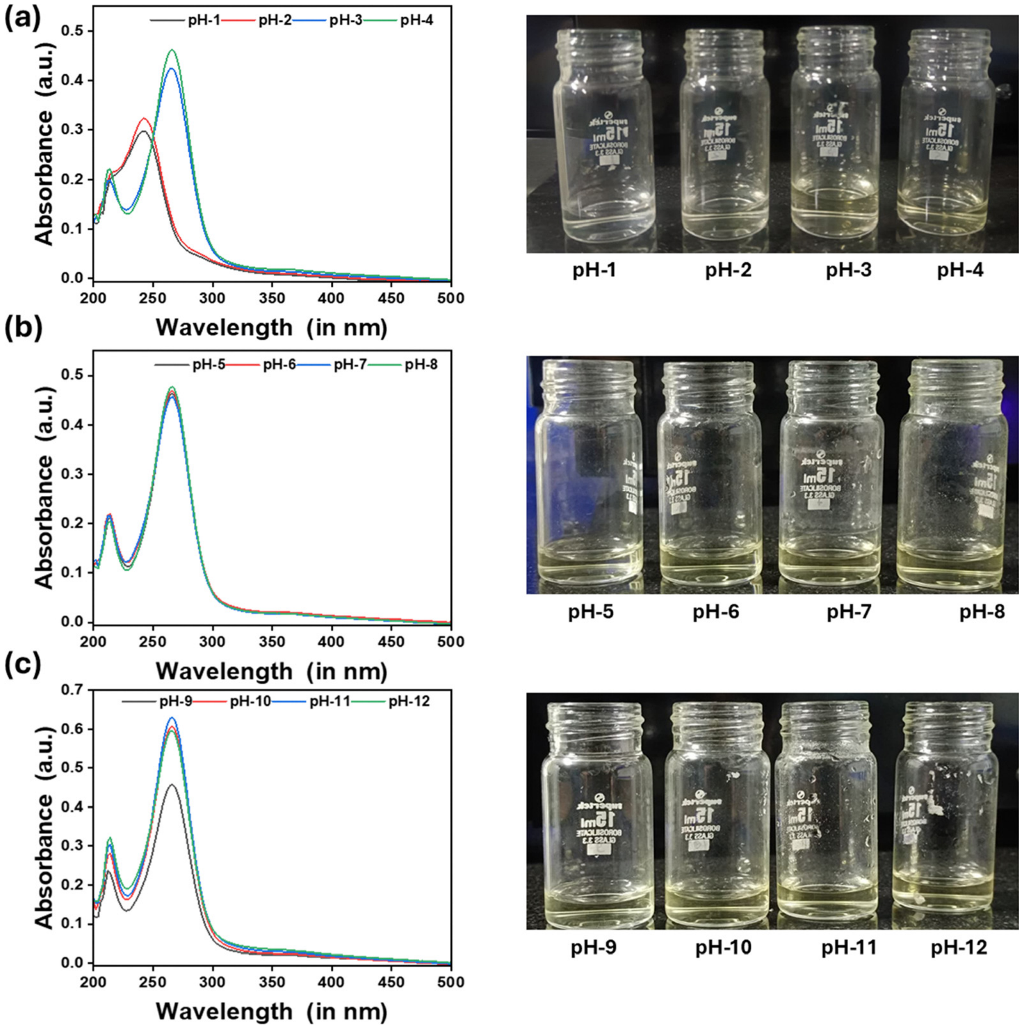

Fig. 3 The absorbance of the GCDs at various pH levels. In the spectra, the *y*-axis represents absorbance, and the *x*-axis represents wavelength. And on the right side, the image shows the GCDs dispersed in different pH solutions. Figures (a)–(c) show fluorescence spectra in different pH ranges.

4. Stability of the GCDs

4.1. Effect of pH *vs.* absorbance of the GCDs

The UV-vis absorbance spectra of the GCDs at different pH values, along with photographs of the dispersions, cover a pH range from 1 to 12. Fig. 3(a) presents data for pH values from 1 to 4, where the spectra show two characteristic absorption peaks: one near 230 nm and a broader band around 270 nm. The absorbance at 270 nm is weakest at pH 1 and 2, increases at pH 3, and reaches its highest value among the acidic samples at pH 4. The image indicates that as pH increases, the colour of the GCD samples changes. The solutions are nearly colourless at pH 1 and 2, while at pH 3 and 4, they appear slightly more intense, suggesting improved optical activity as the medium becomes less acidic. Fig. 3(b) displays the results for pH values 5 to 8, where all spectra nearly completely overlap, showing a strong and consistent peak at approximately 270 nm. The images also demonstrate that the dispersions remain clear and uniform, highlighting the excellent stability of the GCDs in near-neutral conditions. Fig. 3(c) shows the behaviour of GCDs at pH values from 9 to 12, where the absorbance gradually increases with alkalinity, reaching its maximum at pH 12. A faint yellow colouration and slight turbidity are visible in the image at pH 11 and 12, indicating minor aggregation under strong basic conditions. Overall, the data confirm that GCDs exhibit the lowest absorbance in strong acid, maintain strong absorption from pH 5 to 10, and show the highest absorbance at pH 11, as shown in Fig. 3.

4.2. Effect of pH *vs.* fluorescence emission of the GCDs.

We also evaluated the photostability of carbon quantum dots at various pH levels, ranging from 1 to 12, as shown in Fig. 4. The left side of the figure displays the fluorescence spectra, while the right side presents samples exposed to UV light, which exhibit green fluorescence at different pH levels. In Fig. 4(a),

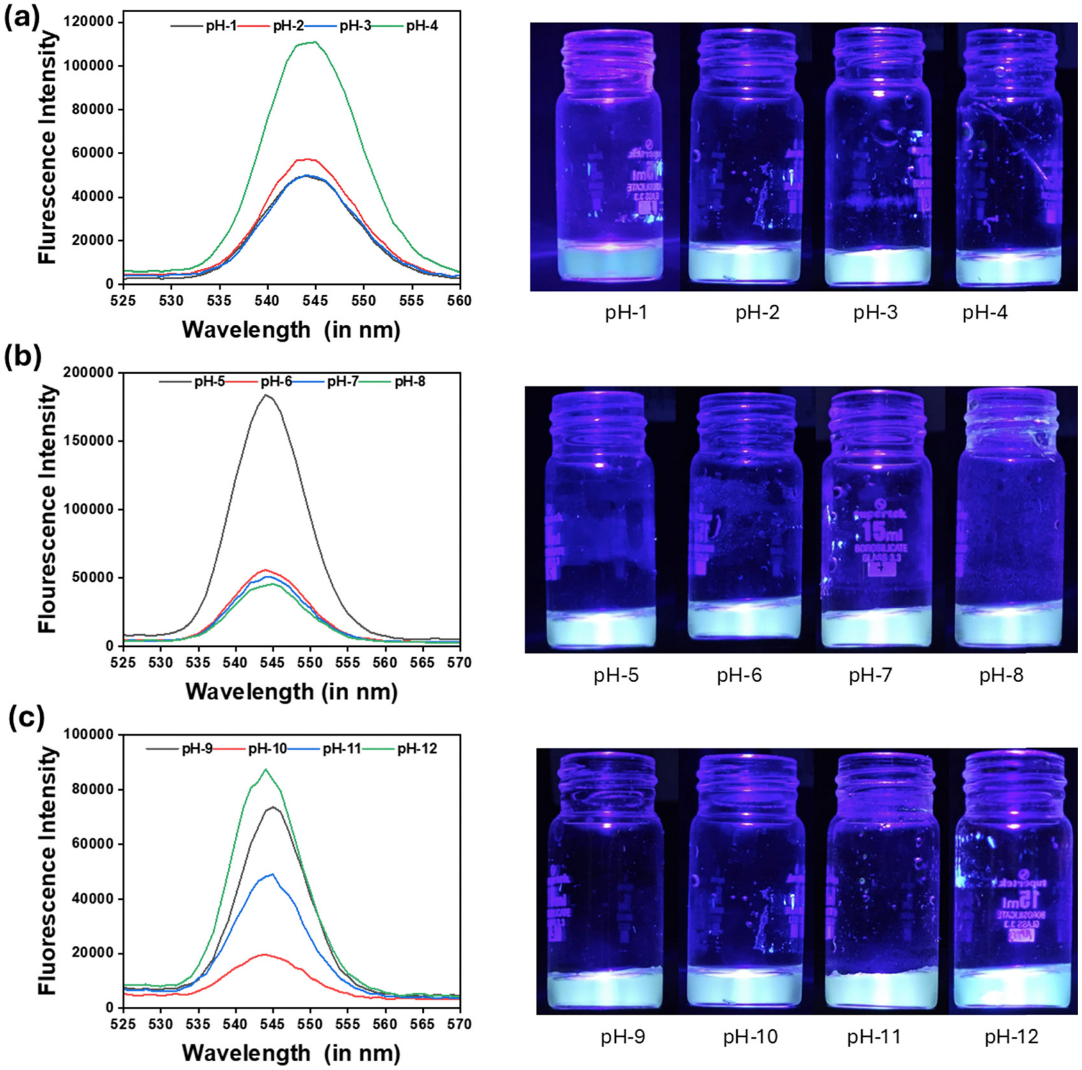

Fig. 4 The fluorescence of the GCDs at different pH levels. In the fluorescence spectra, the *x*-axis represents the wavelength, and the *y*-axis represents the fluorescence intensity. Figures (a)–(c) show the fluorescence intensity of the GCDs at different pH levels, and on the right-hand side, the GCDs are exposed to UV light, and the image shows the green fluorescence.

we observe that in the pH range of 1 to 3, the fluorescence spectra overlap. However, as the pH increases to 4, there is a noticeable increase in fluorescence intensity. While the fluorescence intensity remains consistent at acidic pH levels, it begins to rise once the pH reaches the 4 range. In Fig. 4(b) and (c), at pH 5, the GCDs show maximum fluorescence intensity, and in the pH range 6–7, the fluorescence spectra overlap; this means that at neutral pH, the GCDs are stable, and the neutral pH range shows excellent fluorescence stability. In the pH range 9–12, we can observe the alteration in fluorescence intensity. Finally, Fig. 5 concludes that the neutral pH range is the one in which the GCDs show stable fluorescence intensity, and maximum fluorescence intensity is observed at pH 5.

4.3. Fluorescence stability in different solvents

The fluorescence stability of the GCDs in different solvents over 5 days is illustrated. Fig. 5(a) shows the relative fluorescence intensity of the GCDs dispersed in Milli-Q water, ethanol, PBS, serum-free medium (SFM), and complete medium (CM) over five days. The results indicate that the GCDs maintain excellent fluorescence stability in all solvents, with ethanol and CM showing the most consistent fluorescence intensity throughout the study period. In contrast, minor fluctuations are observed in Milli-Q water and PBS, while SFM shows a slight decrease initially but recovers over time. Fig. 5(b) displays the visual appearance of GCD dispersions in different solvents after incubation. Overall, the results confirm that the GCDs possess remarkable fluorescence stability in various solvents, with ethanol and CM providing the most favourable environment for preserving their optical properties.

5. *In vitro* study

5.1. Cytotoxicity study of the GCDs

Since understanding the cytotoxic effect of the GCDs in normal (non-cancerous) cells and cancer cells is crucial, cytotoxicity was studied using an MTT assay. The experiment was performed in both cancerous (MDA-MB-231) and non-cancerous (RPE1) cell lines.

Fig. 6 shows the effect of different concentrations of GCDs on the viability of two cell lines: RPE1 (Fig. 6(a)) and MDA-MB231 (Fig. 6(b)). The cell viability was not significantly decreased in both cells at even higher concentrations, which suggests that the GCDs are non-toxic. Overall, these results suggest that the GCDs are non-toxic in normal cells and could be used in biomedical applications, specifically for bioimaging.

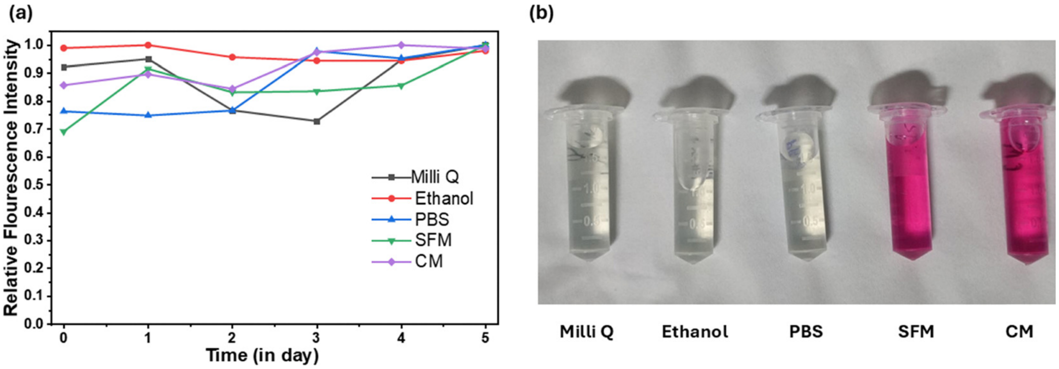

Fig. 5 Fluorescence stability of GCDs in different solvents. (a) Fluorescence spectra; the *y*-axis represents the relative fluorescence, and the *x*-axis represents time. (b) GCDs dissolved in different solvent (left to right) – Milli Q, ethanol, phosphate buffer saline (PBS), serum-free media (SFM), complete media (CM).

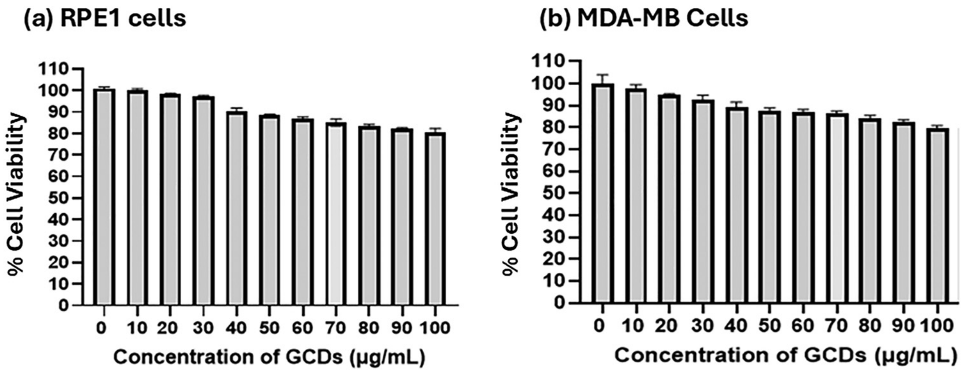

Fig. 6 Cytotoxicity of the GCDs in normal mice RPE1 cells (a) and cancerous MDA-MB-231 cells (b).

5.2. Cellular uptake of the GCDs

Literature reports indicate that GCDs can internalize into cells within 20 minutes.[33,34] Based on this, we hypothesized that the GCDs could be highly up taken by cancer cells. For that assessment, cellular uptake was performed using confocal microscopy.

Confocal images show concentration-dependent internalization of GCDs in RPE1 cells (Fig. 7). The fluorescence intensity of the GCDs in RPE1 cells was quantified. Quantitative data also suggested that normal cells (RPE1) showed lower cellular uptake at 50 μg ml^{-1} and this was increased with respect to concentration. However, compared to cancer cells (MDA-MB-231), the uptake is lowered in non-cancer cells (Fig. 8). Cancer cells showed stronger fluorescence than normal cells. GCD uptake increased at 100 and 200 μg mL^{-1} concentrations, higher than the 50 μg mL^{-1} and the untreated control.

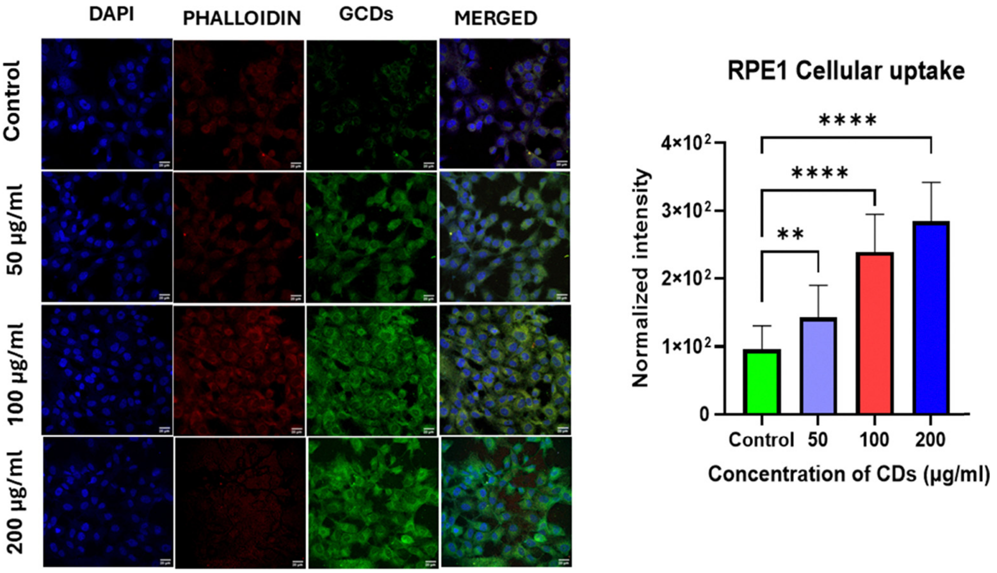

Fig. 7 Cellular uptake of GCDs in RPE1 Cells. The scale bar is 20 μm. Cells were treated with concentrations of GCDs of 50 μg mL^{-1}, 100 μg mL^{-1}, and 200 μg mL^{-1} in RPE1 cells. Cells were stained with DAPI and Phalloidin A647 and observed under confocal microscopy. Statistical significance was assessed using one-way ANOVA in Prism Software, indicated as **** for p-values < 0.0001, highlighting significant differences among the means ($p < 0.05$).

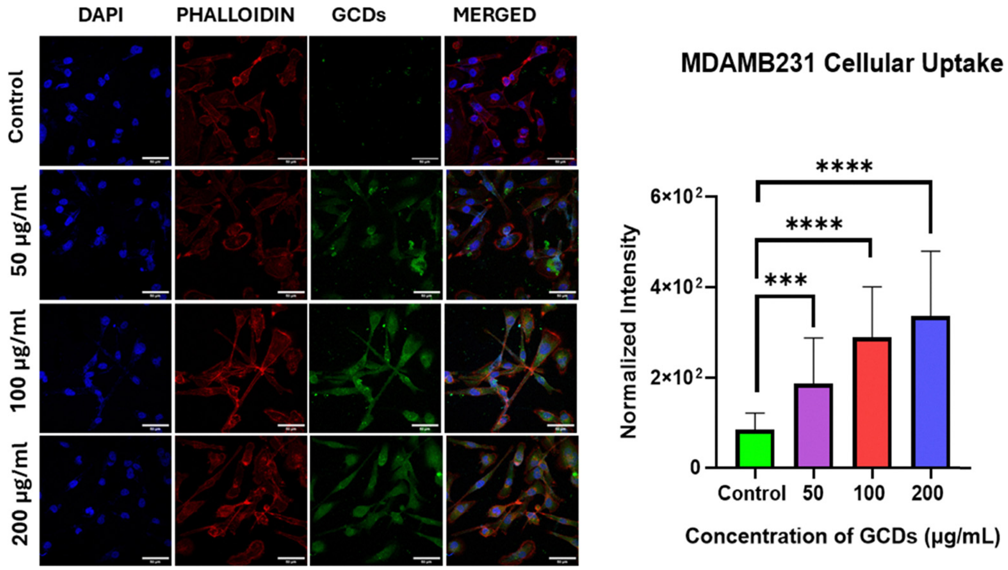

Fig. 8 Cellular uptake of GCDs in MDA-MB-231 cells. The scale bar is 20 μm. Cells were treated with different concentrations of the GCDs (50 μg mL^{-1}, 100 μg mL^{-1}, and 200 μg mL^{-1}). The cells were stained with DAPI and Phalloidin A647 and observed under a confocol microscope. Statistical significance was assessed using one-way ANOVA in Prism Software, indicated as **** for p-values < 0.0001, highlighting significant differences among the means ($p < 0.05$).

5.3. Comparative cellular uptake study of GCDs vs FITC dye fluorescence intensity

To investigate the fluorescence intensity potential of GCDs and to compare their fluorescence intensity with that of the commercially available FITC dye. Both GCDs and FITC were incubated in two different cell lines, RPE1 and HeLa, at the same concentrations of 100 μg ml^{-1} and 200 μg ml^{-1}. RPE1 cells were incubated with GCDs and FITC. We compared the control group with different concentrations: 100 GCDs, 100 FITC, 200 GCDs, and 200 FITC. We quantified the fluorescence intensity and noted significant differences among the groups. Furthermore, the comparison between 100 GCDs and 200 GCDs, as well as between 200 GCDs and 200 FITC, showed significant differences in fluorescence intensity. Lastly, the comparison between 200 GCDs and 200 FITC also revealed significant differences. Based on these results, we can conclude that GCDs demonstrate good fluorescence intensity; however, FITC is more efficient than GCDs (Fig. 9–11).

HeLa cells were incubated with GCDs and FITC. We compared the control group with different concentrations: 100 μg mL^{-1} GCDs, 100 μg mL^{-1} FITC, 200 μg mL^{-1} GCDs, and 200 μg mL^{-1} FITC. We quantified the fluorescence intensity and noted significant differences among the groups. Furthermore, the comparison between 100 μg mL^{-1} GCDs and 200 μg mL^{-1} GCDs, as well as between 200 μg mL^{-1} GCDs and 200 μg mL^{-1} FITC, showed significant differences in fluorescence intensity. Lastly, the comparison between 200 GCDs and 200 μg mL^{-1} FITC also revealed no significant differences. Based on these results, we can conclude that GCDs demonstrate good fluorescence intensity; however, FITC is more efficient than GCDs.

5.4. Selection between healthy and cancerous cells of GCDs

To evaluate GCDs' selectivity, five different types of normal and cancer cell lines were used. In that, two were cancer cells (MDA-MB-231 and HeLa) and three were normal cells (RPE1, NIH3T3, and HeK293). They all were separately incubated with 200 μg ml^{-1} in a four-well plate, then washed three times with 1× PBS. After fixation and staining, the cells were observed under a confocal microscope. As shown in Fig. 6, all cancerous cells stained with GCDs emitted bright fluorescence emission, whereas all normal cells emitted weaker fluorescence. Furthermore, the fluorescence signals were quantified using ImageJ software, and the resulting data were plotted for analysis. The fluorescence intensity in cancer cells was found to be significantly higher than in normal cells, which correlated well with the observations from confocal microscopy images. Additionally, the varying fluorescence emission intensities among different cancer cells might be attributed to their distinct

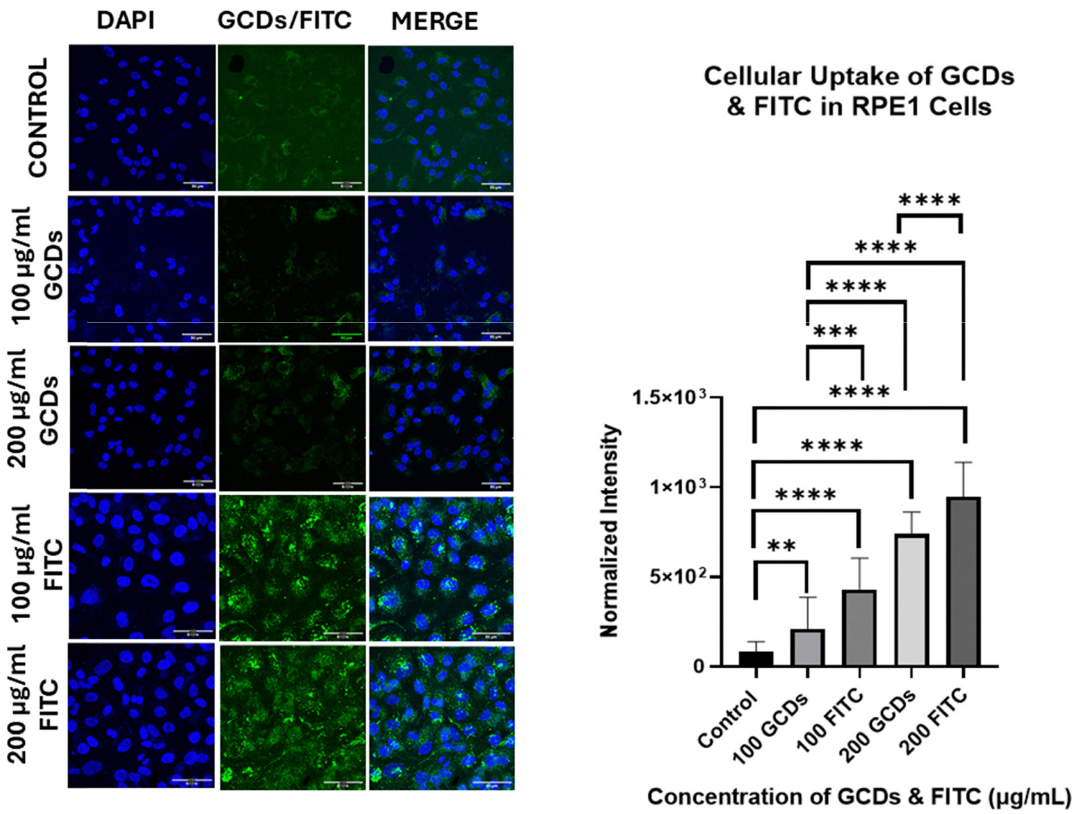

Fig. 9 Cellular uptake of GCDs and FITC in RPE1 cells. The scale bar is 50 μm. Cells were treated with different concentrations of the GCDs (100 μg mL^{-1} and 200 μg mL^{-1}) and FITC (100 μg mL^{-1} and 200 μg mL^{-1}). Cells were stained with DAPI and observed under a confocal microscope. Statistical significance was assessed using one-way ANOVA in Prism Software, indicated as **** for p-values <0.0001, highlighting significant differences among the means ($p < 0.05$).

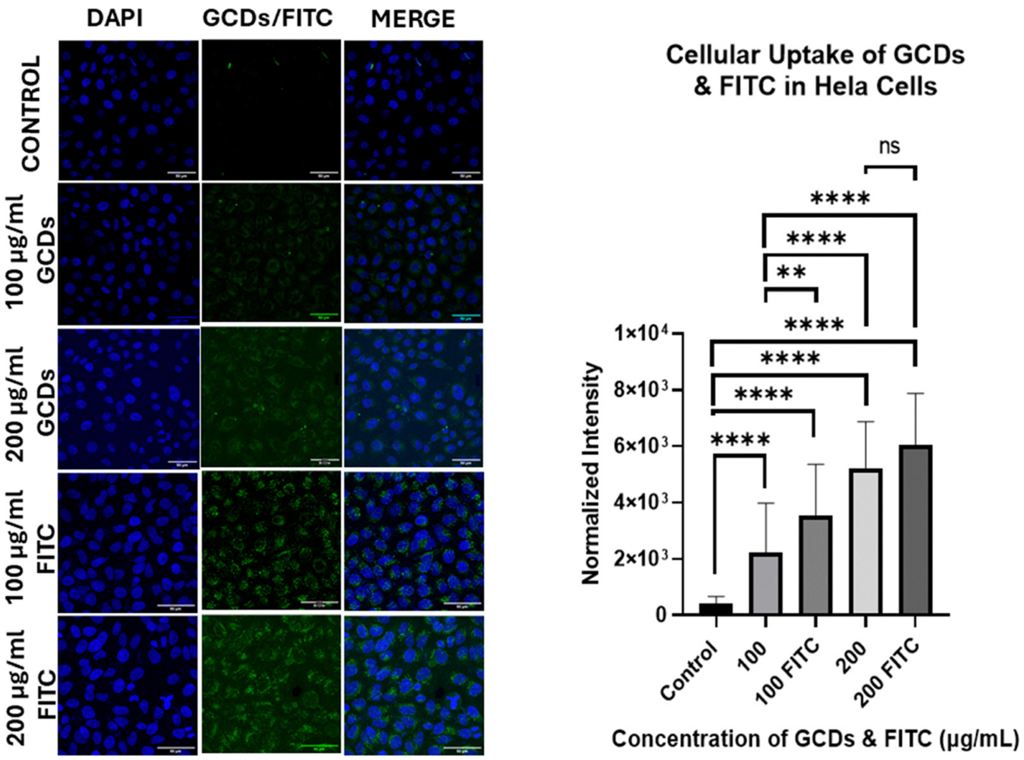

Fig. 10 Cellular uptake of GCDs and FITC in HELA cells. The scale bar is 50 μm. Cells were treated with different concentrations of the GCDs (100 μg mL^{-1} and 200 μg mL^{-1}) and FITC (100 μg mL^{-1} and 200 μg mL^{-1}). Cells were stained with DAPI and observed under a confocal microscope. Statistical significance was assessed using one-way ANOVA in Prism Software, indicated as **** for p-values < 0.0001, highlighting significant differences among the means ($p < 0.05$).

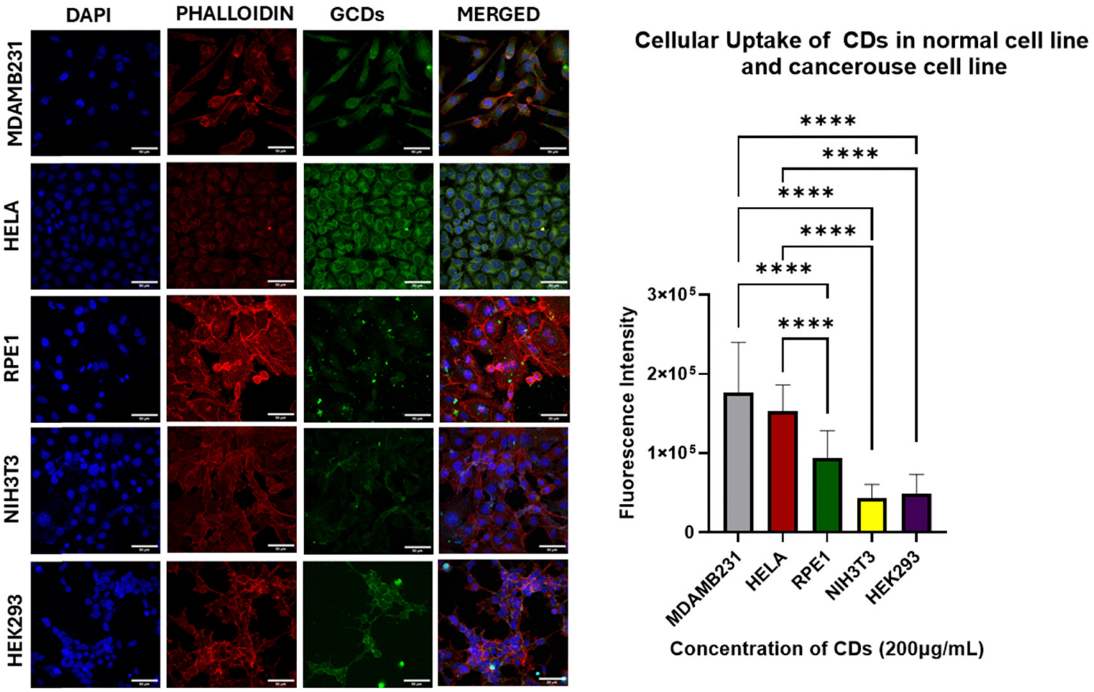

Fig. 11 Cellular uptake of GCDs in different types of cells. Cancerous cells (MDA-MB-231 and HeLa) and normal cells (RPE1, NIH3T3, and HEK293) were treated with GCDs at a 200 μg mL^{-1} concentration and observed under a confocal microscope followed by fixation. Statistical significance was assessed using one-way ANOVA in Prism Software, with results represented as **** when the p-value is less than 0.0001, indicating a significant difference among means at $p < 0.05$. The scale bar is 50 μm.

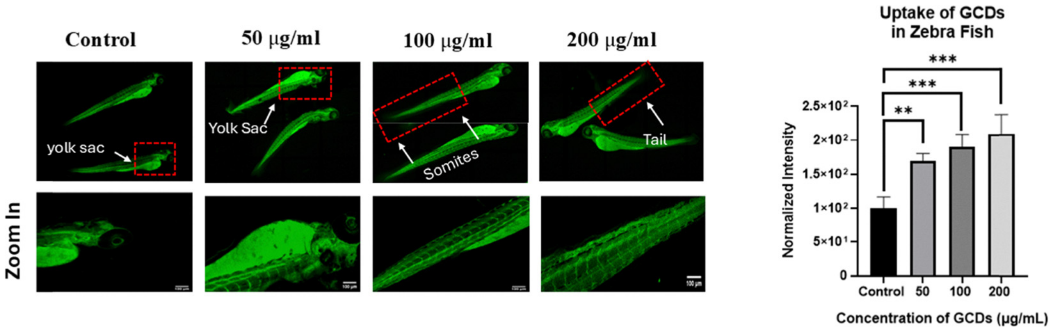

Fig. 12 This study examines the uptake of different concentrations of GCDs in zebrafish larvae at 72 hours post-fertilisation (hpf) after treatment times of 4 hours. During the 4-hour treatment, we observed the accumulation of GCDs in the zebrafish larvae. Fluorescence intensity was measured, and a quantitative analysis of the uptake of various concentrations of GCDs was performed in the 72 hpf zebrafish larvae, with a scale bar set at 100 μm for reference. Statistical significance was indicated with a *p*-value of less than 0.0001 (***) for highly significant results and a *p*-value of less than 0.05 (*) for significant results. A total of 5 larvae per condition were quantified in this analysis.

$\Delta\Psi m$ membrane potential and metabolic rates.[35] These findings suggest that GCDs hold potential as effective probes for distinguishing between normal and cancerous cells, particularly for early cancer detection.

6. *In vivo* study

6.1. Uptake of GCQDs in zebrafish larvae

To investigate the potential of *in vivo* imaging using GCDs, we examined the uptake of GCDs in zebrafish larvae at 72 hours post-fertilisation (hpf). The larvae were exposed to GCDs at different concentrations (50 μg mL^{-1}, 100 μg mL^{-1}, and 200 μg mL^{-1}) for 4 hours. After this incubation period, the uptake of GCDs was significantly higher in all treated groups (50 μg mL^{-1}, 100 μg mL^{-1}, and 200 μg mL^{-1}) compared to the control group. Moreover, the uptake increased with higher concentrations, indicating greater bioavailability of these nanoformulations in the larvae. At 4 hours post-treatment, we observed significantly higher fluorescence intensity of the GCDs in the yolk sac, tail region, and somites of the larvae, particularly at concentrations of 100 and 200 μg mL^{-1}, as shown in Fig. 12.

7. Conclusion

Green, fluorescent carbon dots were successfully synthesized *via* a reflux method using citric acid and ascorbic acid as precursors. These GCDs exhibit selective targeting of cancer cells and can differentiate between cancerous and normal cells. The formation of GCDs was confirmed through a visual test, where they exhibited green fluorescence under UV light. To further characterize their optical and photoluminescent properties, UV-vis spectroscopy and fluorescence spectrophotometry were utilized.

The size and surface characteristics of the GCDs were analyzed using dynamic light scattering (DLS), which revealed a hydrodynamic radius ranging from 2 to 6 nm. Surface charge measurements indicated a pH-dependent trend: as the pH increased, the surface charge became more negative. FTIR spectroscopy confirmed the successful synthesis of the GCDs. X-ray Photoelectron Spectroscopy (XPS) analysis showed that the prepared GCDs are predominantly composed of carbon (C: 58.57%) and oxygen (O: 41.08%), with trace amounts of nitrogen (N: 0.21%) and sulfur (S: 0.15%). Atomic Force Microscopy (AFM) revealed that the GCDs possess a spherical morphology with sizes ranging from 3 to 10 nm. High-resolution transmission electron microscopy (HRTEM) analysis indicated that the synthesized GCDs are spherical, uniformly dispersed, and free from aggregation, with distinct lattice fringes exhibiting an interplanar spacing of approximately 0.26 nm. The size distribution shows that most particles cluster around 3 to 4 nm, confirming a well-defined core and consistent size distribution. The MTT assay suggests that the prepared GCDs are biocompatible with normal cells, while significantly killing cancer cells. Cellular uptake studies demonstrated that GCDs were internalized more efficiently by cancer cells than by normal cells, indicating their selective targeting capabilities. Additionally, when comparing the cellular uptake and fluorescence intensity of the GCDs with FITC, it was reported that FITC showed significantly more uptake and intensity. In further experiments involving five different cancerous and normal cell lines incubated with 200 μg mL^{-1} of GCDs, the cancer cells exhibited significantly higher fluorescence intensity compared to normal cells. These findings confirm the selective ability of GCDs to differentiate between cancerous and normal cells. Moreover, to investigate the uptake of GCDs in an *in vivo* model, zebrafish studies showed a significant increase in uptake as the concentration of GCDs increased. This study suggests that GCDs have potential applications as fluorescent probes in biomedical settings, particularly in cancer diagnostics. However, further research should focus on the selectivity and biocompatibility of GCDs in *in vivo* models for more validation.

Conflicts of interest

There are no conflicts to declare.

Data availability

No code or algorithms were developed for this manuscript. The raw data files like DLS, AFM, Confocal microscope images and the subsequent quantification data can be provided upon request from the authors.

Acknowledgements

We sincerely thank all members of the DB Lab at IITGN for their valuable discussions and contributions. We appreciate the Central Instrumentation Facility at IITGN for providing the necessary infrastructure. DB expresses gratitude to ANRF-CRG, GSBTM, and MoES-STARS for their research funding. RS acknowledges Anusandhan National Research Foundation (ANRF) for the National Post-Doctoral Fellowship (N-PDF).

References

1 D. Crosby, *et al.*, Early detection of cancer, *Science*, 2022, **375**, aay9040.
2 F. Bray, *et al.*, Global cancer statistics 2022: GLOBOCAN estimates of incidence and mortality worldwide for 36 cancers in 185 countries, *Ca-Cancer J. Clin.*, 2024, **74**, 229–263.
3 T. P. M. Daby, U. Modi, A. K. Yadav, D. Bhatia and R. Solanki, Bioimaging and therapeutic applications of multifunctional carbon quantum dots: Recent progress and challenges, *Next Nanotechnol.*, 2025, **8**, 100158.
4 World Health Organization (WHO). https://www.who.int/.
5 S. Luo, E. Zhang, Y. Su, T. Cheng and C. Shi, A review of NIR dyes in cancer targeting and imaging, *Biomaterials*, 2011, **32**, 7127–7138.
6 S. Y. Xiao, *et al.*, Application of fluorescein sodium in breast cancer brain-metastasis surgery, *Cancer Manage. Res.*, 2018, **10**, 4325–4331.
7 S. Thevarajah, T. L. Huston and R. M. Simmons, A comparison of the adverse reactions associated with isosulfan blue versus methylene blue dye in sentinel lymph node biopsy for breast cancer, *Am. J. Surg.*, 2005, **189**, 236–239.
8 H. Wang, *et al.*, Indocyanine green-incorporating nanoparticles for cancer theranostics, *Theranostics*, 2018, **8**, 1227.
9 Y. Canitrot, S. Lahmy, J. J. Buquen, D. Canitrot and D. Lautier, Functional study of multidrug resistance with fluorescent dyes. Limits of the assay for low levels of resistance and application in clinical samples, *Cancer Lett.*, 1996, **106**, 59–68.
10 J. M. Warram, *et al.*, Antibody-based imaging strategies for cancer, *Cancer Metastasis Rev.*, 2014, **33**, 809–822.
11 C. A. Metildi, *et al.*, Fluorescence-guided surgery with a fluorophore-conjugated antibody to carcinoembryonic antigen (CEA), that highlights the tumor, improves surgical resection and increases survival in orthotopic mouse models of human pancreatic cancer, *Ann. Surg. Oncol.*, 2014, **21**, 1405–1411.
12 H. Wang, *et al.*, Advances in Prostate-Specific Membrane Antigen (PSMA)-Targeted Phototheranostics of Prostate Cancer, *Small Struct.*, 2022, **3**, 2200036.
13 H. Kobayashi, P. L. Choyke and M. Ogawa, Monoclonal antibody-based optical molecular imaging probes; considerations and caveats in chemistry, biology and pharmacology, *Curr. Opin. Chem. Biol.*, 2016, **33**, 32.
14 Á. Szabó, *et al.*, The Effect of Fluorophore Conjugation on Antibody Affinity and the Photophysical Properties of Dyes, *Biophys. J.*, 2018, **114**, 688.
15 Immunofluorescence - Types, Techniques, and Limitations - New York Microscope Company. https://microscopeinternational.com/immunofluorescence/.
16 Q. Yu, *et al.*, Cathepsin B Activatable Fluorescent Probe for Antitumor Efficiency Feedback: Attempt To Detect Certain Apoptotic Cells, *Anal. Chem.*, 2025, **97**, 2932–2940.
17 H. W. Liu, *et al.*, Recent progresses in small-molecule enzymatic fluorescent probes for cancer imaging, *Chem. Soc. Rev.*, 2018, **47**, 7140–7180.
18 P. M. Boiselle, Computed Tomography Screening for Lung Cancer, *JAMA*, 2013, **309**, 1163–1170.
19 S. H. Bradley, *et al.*, Sensitivity of chest X-ray for detecting lung cancer in people presenting with symptoms: a systematic review, *Br. J. Gen. Pract.*, 2019, **69**, e827–e835.
20 B. Blasiak, F. C. J. M. Van Veggel and B. Tomanek, Applications of Nanoparticles for MRI Cancer Diagnosis and Therapy, *J. Nanomater.*, 2013, **2013**, 148578.
21 R. Guo, G. Lu, B. Qin and B. Fei, Ultrasound Imaging Technologies for Breast Cancer Detection and Management: A Review, *Ultrasound Med. Biol.*, 2018, **44**, 37–70.
22 A. Sharma and D. D. Bhatia, Programmable bionanomaterials for revolutionizing cancer immunotherapy, *Biomater. Sci.*, 2024, **12**, 5415–5432.
23 F. W. Pratiwi, C. W. Kuo, B. C. Chen and P. Chen, Recent Advances in the use of Fluorescent Nanoparticles for Bioimaging, *Nanomedicine*, 2019, **14**, 1759–1769.
24 A. Kumar, *et al.*, Clinical Applications of Targeted Nanomaterials, *Pharmaceutics*, 2025, **17**, 379.
25 D. Benner, P. Yadav and D. Bhatia, Red emitting carbon dots: surface modifications and bioapplications, *Nanoscale Adv.*, 2023, **5**, 4337–4353.
26 A. Kumar, *et al.*, Next-Generation Cancer Theragnostic: Applications of Carbon Quantum Dots, *ChemNanoMat*, 2025, **11**, e202500061.
27 A. Kumar, *et al.*, Clinical Applications of Targeted Nanomaterials, *Pharmaceutics*, 2025, **17**, 379.
28 T. Bhattacharya, G. H. Shin and J. T. Kim, Carbon Dots: Opportunities and Challenges in Cancer Therapy, *Pharmaceutics*, 2023, **15**, 1019.
29 B. Ghaemi and M. Javad Hajipour, Tumor acidic environment directs nanoparticle impacts on cancer cells, *J. Colloid Interface Sci.*, 2023, **634**, 684–692.
30 C. L. Shen, *et al.*, Recent progress of carbon dots in targeted bioimaging and cancer therapy, *Theranostics*, 2022, **12**, 2860.

31 K. Das, *et al.*, Divergent Responses of Hydrophilic CdSe and CdSe@CdS Core–Shell Nanocrystals in Apoptosis and *In Vitro* Cancer Cell Imaging: A Comparative Analysis, *J. Funct. Biomater.*, 2023, **14**, 448.

32 P. Yadav, *et al.*, Tissue-Derived Primary Cell Type Dictates the Endocytic Uptake Route of Carbon Quantum Dots and *In Vivo* Uptake, *ACS Appl. Bio. Mater.*, 2023, **6**, 1629–1638.

33 L. W. Zhang and N. A. Monteiro-Riviere, Mechanisms of Quantum Dot Nanoparticle Cellular Uptake, *Toxicol. Sci*, 2009, **110**, 138–155.

34 Y. Xiao, *et al.*, Dynamics and mechanisms of quantum dot nanoparticle cellular uptake, *J. Nanobiotechnol.*, 2010, **8**, 13.

35 H. M. Begum and K. Shen, Intracellular and microenvironmental regulation of mitochondrial membrane potential in cancer cells, *WIREs Mech. Dis.*, 2023, **15**, e1595.